Enhanced Catalytic Ozonation for Eliminating CH$_3$SH via Graphene-Supported Positively Charged Atomic Pt Undergoing Pt^{2+}/Pt^{4+} Redox Cycle

Yajing Huang, Dingren Ma, Weiqi Liu, Dehua Xia,* Lingling Hu, Jingling Yang, Peng Liao, and Chun He

Read Online

ACCESS | Metrics & More | Article Recommendations | SI Supporting Information

ABSTRACT: Constructing catalysts with electronic metal−support interaction (EMSI) is promising for catalytic reactions. Herein, graphene-supported positively charged (Pt^{2+}/Pt^{4+}) atomically dispersed Pt catalysts (AD-Pt-G) with Pt$_x$C$_3$ (x = 1, 2, and 4)-based EMSI coordination structures are achieved for boosting the catalytic ozonation for odorous CH$_3$SH removal. A CH$_3$SH removal efficiency of 91.5% can be obtained during catalytic ozonation using optimum 0.5AD-Pt-G within 12 h under a gas hourly space velocity of 60,000 mL h^{-1} g^{-1}, whereas that of pure graphene is 40.4%. Proton transfer reaction time-of-flight mass spectrometry, *in situ* diffuse reflectance infrared Fourier transform spectroscopy/Raman, and electron spin resonance verify that the Pt$_x$C$_3$ coordination structure with atomic Pt^{2+} sites on AD-Pt-G can activate O$_2$ to generate peroxide species (*O$_2$) for partial oxidation of CH$_3$SH during the adsorption period and trigger O$_3$ into surface atomic oxygen (*O$_{ad}$), *O$_2$, and superoxide radicals (·O$_2^-$) to accomplish a stable, high-efficiency, and deeper oxidation of CH$_3$SH during the catalytic ozonation stage. Moreover, the results of XPS and DFT calculation imply the occurrence of Pt^{2+} → Pt^{4+} → Pt^{2+} recirculation on Pt$_x$C$_3$ for AD-Pt-G to maintain the continuous catalytic ozonation for 12 h, i.e., Pt^{2+} species devote electrons in 5d-orbitals to activate O$_3$, while Pt^{4+} species can be reduced back to Pt^{2+} via capturing electrons from CH$_3$SH. This study can provide novel insights into the development of atomically dispersed Pt catalysts with a strong EMSI effect to realize excellent catalytic ozonation for air purification.

KEYWORDS: *atomically dispersed Pt, catalytic ozonation, Pt^{2+} → Pt^{4+} → Pt^{2+} recirculation, methyl mercaptan, electronic metal−support interaction*
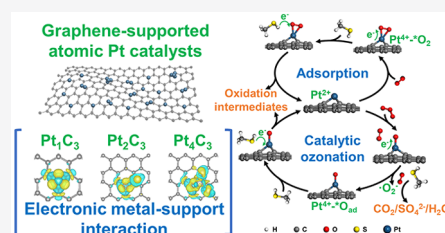
1. INTRODUCTION

As one of the main contributors to malodorous pollution, the elimination of sulfur-containing volatile organic compounds (SVOCs) like methyl mercaptan (CH$_3$SH) has attracted increasing public attention.[1,2] With the concentrations ranging from tens to hundreds of ppm, CH$_3$SH with an ultralow olfactory threshold exists widely in the petroleum industry, sewage/waste water treatment plants, and sanitary landfill.[3−5] High concentrations of CH$_3$SH can poison the human nervous system, cause acid rain, corrode reactors, and inactivate catalysts in chemical industry.[5,6] Hence, numerous techniques have been investigated to remove CH$_3$SH such as adsorption,[7,8] biological degradation,[9] catalytic oxidation,[10] photocatalytic oxidation,[11,12] and catalytic ozonation.[13] Especially, catalytic ozonation is an effective and economic technology for the removal of SVOCs owing to its high efficiency, enhanced mineralization, and mild operation conditions.[14,15] To achieve the efficient and complete SVOCs removal, it is necessary to develop highly active catalysts for catalytic ozonation to eliminate CH$_3$SH.

Supported Pt-based catalysts are considered as high-performance catalysts for catalytic ozonation owing to their unoccupied 5d-orbitals and strong adsorption/activation ability for reactants.[16,17] However, their practical performance is still hampered by the low dispersion of active sites and insufficient catalytic activity.[17,18] Actually, constructing a strong electronic metal−support interaction (EMSI) for supported metal catalysts can solve these two issues simultaneously.[19−21] For one thing, the EMSI effect is beneficial to the dispersion and stabilization of the supported metals into sub-nanometer clusters or even atomically dispersed atoms.[19,20] For another, EMSI can also regulate the electronic properties and d-band center of active sites as well as the adsorption for reactants and intermediates, thus leading to an excellent catalytic activity.[22] Especially, carbon supports with versatile structures and conductive properties are more likely to induce the EMSI effect since they can substantially influence the geometric configuration, electronic structure, and interaction with the metal catalysts.[20,23] For instance, the carbon defects on graphene are beneficial to

stabilizing the atomic Pt_1C_3 coordination environment via a covalent Pt−C bond with a higher binding energy so as to construct Pt-based atomically dispersed catalysts (Pt-ADCs) and maximize the EMSI effect.[24] In addition, the excellent electrical conductivity of delocalized π-electrons in graphene can promote the electron transfer and active-site circulation in catalytic ozonation.[25] Thus, it is still challenging to develop the graphene-supported atomic Pt catalysts with strong EMSI for catalytic ozonation.

Generally, in the catalytic ozonation process, it is essential to improve the adsorption and dissociation ability of catalysts for O_3 and SVOCs molecules. Due to the Lewis basicity of the terminal oxygen atom of O_3 molecules, O_3 tends to be adsorbed on the Lewis acid sites with empty d-orbitals.[26,27] Compared with the widely reported Pt nanoparticle-based catalysts (Pt^0), the construction of graphene-supported Pt-ADCs with EMSI-induced positively charged Pt sites (Pt^{2+}/Pt^{4+}) may promote the formation of Lewis acid sites for O_3 adsorption and the devotion of electrons to activate O_3 during catalytic ozonation.[22,28] Moreover, compared with the redox pair of $Pt^0/Pt^{\delta+}$ (δ = 2 or 4) in nanoparticular Pt catalysts that probably leads to the aggregation of active sites, the redox pair of Pt^{2+}/Pt^{4+} in graphene-supported Pt-ADCs is beneficial to maintaining the dispersion and stability of active species.[22] Importantly, the atomic Pt sites with a higher valence (Pt^{4+}) was also proven to be beneficial to the adsorption of VOCs via trapping electrons, which may also be readily applicable for SVOCs.[29] Furthermore, with the electron-deficient atomic Pt^{4+} sites as electron acceptors and conductive graphene as an electron shutter, graphene-supported Pt-ADCs can maintain high activity via rapid circulation of Pt^{2+}/Pt^4 sites.[30] Therefore, it is desired to develop and construct the graphene-supported Pt-ADCs with a strong EMSI effect for boosting catalytic ozonation to eliminate SVOCs.

In this research, the atomically dispersed Pt species were successfully anchored on the reduced graphene oxide (AD-Pt-G) with the Pt−C covalent bond-based EMSI effect for catalytic ozonation to eliminate CH_3SH. The as-prepared AD-Pt-G samples obtained excellent activity and superior stability for catalytic ozonation over a 12 h long-term test owing to the rapid circulation of the Pt^{2+}/Pt^{4+} redox pair. The catalytic mechanism is investigated by in situ DRIFTS/Raman and DFT calculation. This study can open up a strategy for the development of atomic catalysts in ozonation and air purification.

2. EXPERIMENTAL SECTION

2.1. Preparation of AD-Pt-G. The chemical reagents used in this study are listed in Text S1 of the Supporting Information. The synthesis of graphene oxide (GO) and reduced graphene oxide (rGO) is described in Text S2. To prepare AD-Pt-G, 60 mL of GO aqueous suspension (2 mg mL^{-1}) was first sonicated for 3 h in an ice bath. Then, x μL (x = 64, 128, and 256) of aqueous H_2PtCl_6 solution (5 mg mL^{-1}) was added into the GO suspension followed by stirring for 12 h and sonication for another 15 min. The precursor solution was then freeze-dried to obtain the brown sample followed by annealing at 600 °C for 3 h under N_2 protection at a heating rate of 5 °C min^{-1}. After collecting and washing, the products were dried in vacuum at 40 °C overnight and denoted as xAD-Pt-G (x = 0.25, 0.5, and 1.0), where x represents the weight percentage ratio of platinum to carbon. For example, the weight ratio of platinum to carbon in 0.5AD-Pt-G is

approximately 0.5 wt %. For comparison, the pure graphene was prepared and denoted as PG, and the preparations of 0.5NP-Pt-G, 0.5Pt-CNTs, and 0.5Pt-g-C_3N_4 are listed in Texts S3−S5. The regeneration method of the used catalysts is listed in Text S6.

2.2. Characterization. The morphology of the catalysts was observed with a field-emission scanning electron microscope (FESEM, Quanta 400F, Netherlands) and transmission electron microscopes (TEM, FEI Tecnai G2 Spirit and FEI Tecnai G2 F30, USA). The atomic-scale images of high-angle annular dark-field scanning transmission electron microscopy (HAADF-STEM) of catalysts were collected using spherical aberration-corrected scanning transmission electron microscopes (Cs-corrected STEM, FEI Themis G2 and FEI Themis Z, USA). The X-ray diffraction (XRD) patterns of the catalysts were collected using an X-ray diffractometer (Rigaku UltimaIV, Japan) equipped with Cu Kα radiation. The Pt loadings were determined using an inductively coupled plasma optical emission spectrometer (ICP-OES, Aglient 5110, USA). The chemical compositions of the catalysts were determined with the Al Kα X-ray source using an X-ray photoelectron spectroscope (XPS, ESCALAB 250, Thermo Fisher Scientific, USA). Raman spectra were obtained using a Laser Micro-Raman Spectrometer (Renishaw inVia, UK) with a wavelength of 514.5 nm laser excitation. Electron paramagnetic resonance (EPR) spectra in the solid state were obtained using an electron paramagnetic resonance spectrometer (Bruker A300, Germany) at room temperature. Pt L_3-edge X-ray absorption fine structure (XAFS) spectra were acquired at the National Synchrotron Radiation Research Center in Hsinchu, Taiwan, China, and experimental details are described in Text S7.

2.3. Catalytic Ozonation of CH_3SH. Ozone was generated by an ozone generator (YDG, YE-TG-02PII) from pure oxygen (99.99%), and the inlet concentration was set to be 467 ppm approximately. The catalytic ozonation experiment was conducted in a flow-through quartz reactor with 0.1 g of catalysts under ambient conditions under room temperature (24 °C ± 2 °C) and a relative humidity of 65%, unless otherwise specified. The flow rate of ozone was 10 mL min^{-1}, while the total flow rate of feed gas was kept at 100 mL min^{-1}, equal to a gas hourly space velocity (GHSV) of 60,000 mL h^{-1} g^{-1}. The inlet CH_3SH concentration was controlled at 50 ppm by diluting 1000 ppm of CH_3SH (Air Liquide, balanced using N_2) using clean air or pure nitrogen (99.99%). A CH_3SH sensor (Detcon, DM-400IS, USA) was used to monitor the concentration of CH_3SH in the inlet and outlet gas. A flowmeter and a buffer bottle were placed between the reactor outlet and the CH_3SH sensor to measure the outlet flow rate and protect the sensor, respectively. The 180 min removal efficiency was taken as an index to compare the catalytic performance of different catalysts.

2.4. Analysis and Calculation. The degradation volatile intermediates and products during adsorption and catalytic ozonation were identified by a proton transfer reaction time-of-flight mass spectrometer (PTR-ToF-MS) using a PTR-TOF 1000 instrument (Ionicon Analytik GmbH, Austria). The in situ diffuse reflectance infrared Fourier transform spectroscopy (in situ DRIFTS) was conducted using a Fourier transform infrared spectrometer (Bruker, TENSOR II, Germany). Atomic oxygen and reactive oxygen species (ROS) were analyzed by in situ Raman (Renishaw inVia, UK) and electron spin resonance (ESR, Bruker A300, Germany). The spin-polarized density functional theory (DFT) calculations were
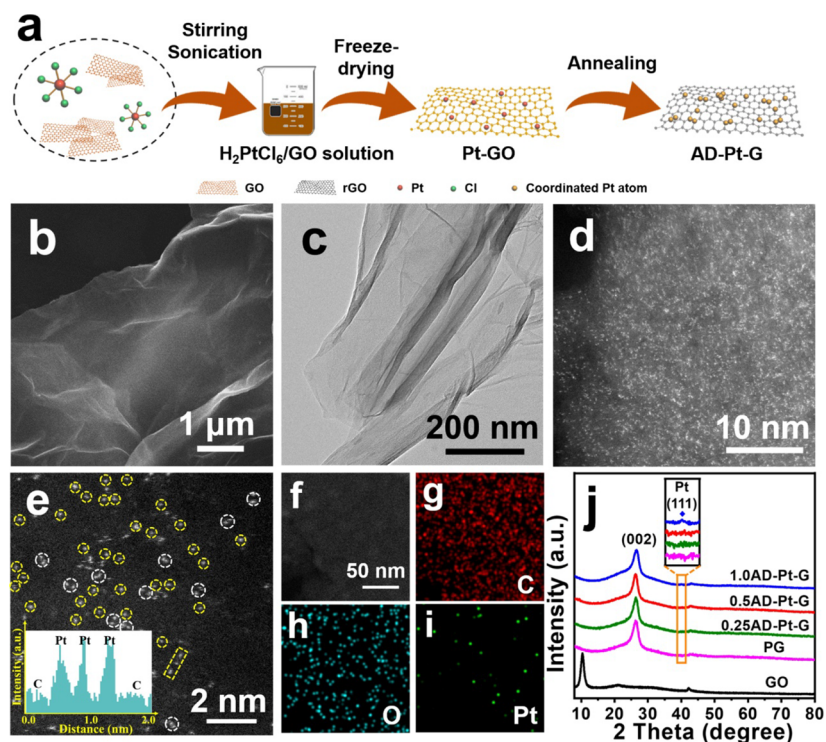
Figure 1. (a) Schematic illustration for the synthesis of AD-Pt-G samples. (b) SEM image, (c) TEM image, (d, e) HAADF-STEM images, and (f–i) element mapping for 0.5AD-Pt-G. (j) XRD patterns for 1.0AD-Pt-G, 0.5AD-Pt-G, 0.25AD-Pt-G, PG, and GO. The yellow and white circles in (e) represent single Pt_1 atoms and Pt_2 dimers, respectively. The inset in Figure 1e shows the intensity profile along the yellow dashed rectangle, demonstrating the dispersion and size of Pt atoms.
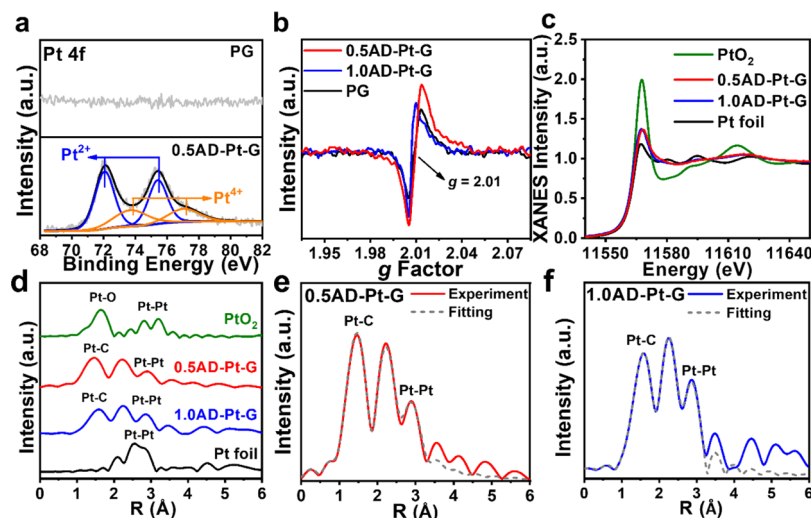

Figure 2. (a) XPS spectra of Pt 4f for PG and 0.5AD-Pt-G samples. (b) Solid-state EPR spectra of PG, 0.5AD-Pt-G, and 1.0AD-Pt-G. (c) Normalized Pt L_3-edge XANES spectra and (d) k^2-weighted FT-EXAFS of 0.5AD-Pt-G, 1.0AD-Pt-G, and references. Fitting results of EXAFS for (e) 0.5AD-Pt-G and (f) 1.0AD-Pt-G.

conducted in the Vienna *ab initio* simulation package (VASP 5.4.1) with the generalized gradient approximation to calculate the adsorption energy (E_{ad}) of CH_3SH, O_2, and O_3 molecules on Pt_xC_3 models including Pt_1C_3, Pt_2C_3, and Pt_4C_3 structures according to the following equation:

$$E_{ad} = E_c - (E_p + E_m) \tag{1}$$

where E_c, E_p, and E_m represent the energies of the adsorption complex, the Pt_xC_3 model, and the individual CH_3SH, O_2, or

O_3 molecule, respectively. The detailed methods for analysis and calculation are listed in Texts S8−S11.

3. RESULTS AND DISCUSSION

3.1. Characterization of AD-Pt-G Catalysts. The atomically dispersed Pt anchored on graphene nanosheet catalysts (AD-Pt-G) were synthesized via a simple freeze-drying and annealing procedure (Figure 1a). The morphology of the as-prepared catalysts was investigated using FESEM, TEM, and HAADF-STEM at first. As shown in Figure 1b,c and
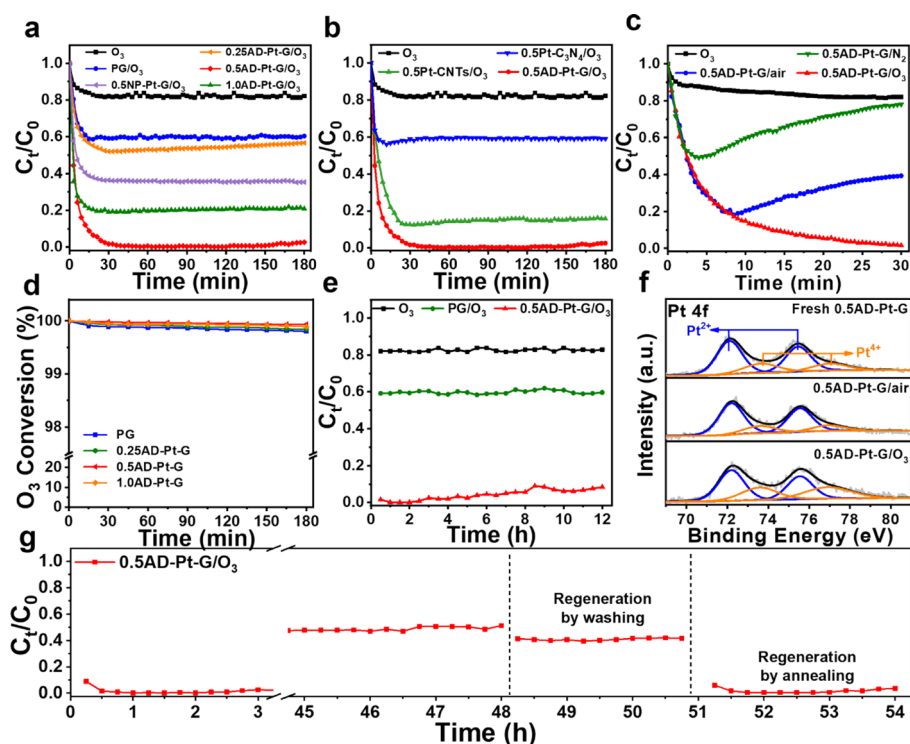
Figure 3. CH_3SH removal in catalytic ozonation using (a) different AD-Pt-G and NP-Pt-G samples, (b) different carbon-supported Pt samples, and (c) in different processes using 0.5AD-Pt-G. (d) O_3 conversion using different AD-Pt-G samples. (e) CH_3SH removal in catalytic ozonation using PG and 0.5AD-Pt-G under a 12 h reaction. (f) Pt 4f XPS spectra of 0.5AD-Pt-G samples after adsorption and catalytic ozonation for CH_3SH removal. (g) CH_3SH removal in catalytic ozonation by continuous use of 0.5AD-Pt-G regenerated by washing or annealing.

Figure S1a,b, the SEM and TEM images of 0.5AD-Pt-G show that 0.5AD-Pt-G exhibits the nanosheet-like surface of graphene with wrinkles, and no obvious Pt nanoparticles are observed on its surface. The HAADF-STEM images (Figure S1c,d) further indicate the smooth surface of graphene nanosheets of 0.5AD-Pt-G. However, as depicted in the atomic resolution HAADF-STEM images (Figure 1d,e and Figure S1e,f), the randomly distributed brighter spots (yellow and white circles in Figure 1e) indicate Pt atoms due to the larger atomic number compared with the carbon atoms of graphene supports, which demonstrates that Pt species are atomically dispersed on the graphene nanosheet of 0.5AD-Pt-G. The randomly measured distances of Pt−Pt atoms suggest that the main atomic Pt species exist as single Pt_1 atoms with distances of 0.3−0.8 nm and Pt_2 dimers with Pt−Pt distances of 0.2−0.3 nm (Figure S2). The energy-dispersive spectroscopy (EDS) mapping results (Figure 1f−i) also show the uniform distribution of C, O, and Pt elements on 0.5AD-Pt-G. Additionally, the TEM and HAADF-STEM images of 0.25AD-Pt-G (Figure S3) prove that there are similar wrinkled graphene layers and a relatively lower density of atomic Pt species dispersed on 0.25AD-Pt-G, due to its lower Pt loading than 0.5AD-Pt-G. Notably, compared with 0.5AD-Pt-G and 0.25AD-Pt-G, the TEM and HAADF-STEM images of 1.0AD-Pt-G (Figure S4) indicate the obvious coexistence of numerous Pt nanoparticles and atomic Pt species on 1.0AD-Pt-G with a higher Pt loading. As for the XRD patterns in Figure 1j, 0.25AD-Pt-G and 0.5AD-Pt-G display no additional peak related to Pt species due to its trace amount and high dispersion on graphene, whereas 1.0AD-Pt-G exhibits a weak peak of Pt(111) at around 40°, consistent with the existence of Pt nanoparticles observed in the HAADF-STEM images of

1.0AD-Pt-G. These results collectively prove the successful preparation of graphene-supported atomically dispersed Pt samples. In addition, the obvious peaks corresponding to Pt(111) and Pt(200) in XRD as well as Pt nanoparticles in TEM for 0.5NP-Pt-G prepared by a chemical reduction method (Figure S5) indicate the abundant existence of Pt nanoparticles on 0.5NP-Pt-G.

XPS was used to further probe the surface element compositions and valence states of atomic Pt on 0.5AD-Pt-G (Figure 2a and Figures S6 and S7). Besides the presence of C and O, the survey spectrum in Figure S6 demonstrates the extra existence of the Pt element on 0.5AD-Pt-G (with 0.06 at % Pt) compared with PG. The deconvolution of the Pt 4f peak of 0.5AD-Pt-G (Figure 2a) indicates that Pt exists in a prominent oxidized state with 72.02% of Pt^{2+} (72.2 eV for Pt $4f_{7/2}$) and 27.98% of Pt^{4+} (73.6 eV for Pt $4f_{7/2}$).[31] The presence of positively charged Pt species rather than Pt^0 species (71.2 eV) verifies that the Pt elements on 0.5AD-Pt-G exist in atomically dispersed states with a strong EMSI effect instead of metallic states, similar to those reports on ADCs.[31−33] In contrast, the major Pt^0 valence state in the Pt 4f spectrum of 0.5NP-Pt-G (Figure S8) indicates the existence of metallic Pt^0 species on 0.5NP-Pt-G with nanoparticular Pt due to the weak interaction between Pt nanoparticles and the graphene support. The positively charged Pt on 0.5AD-Pt-G can be attributed to the Pt−C bond-based EMSI-induced electron transfer from atomic Pt to the graphene support, which can modulate the bond network and electronic structure of graphene.[34,35] This is well evidenced by the Raman spectra of AD-Pt-G (Figure S9), as the G and 2G bands of AD-Pt-G samples show different red shifts compared with that of PG, and 0.5AD-Pt-G presents the largest red shifts of ~4 and ~9

cm^{-1} for the G band and 2G band, respectively.[36] The uneven charge density distribution constructed by the strong Pt−C interaction was further evidenced by solid-state EPR (Figure 2b), as 0.5AD-Pt-G obtains a higher intensity peak than PG and 1.0AD-Pt-G at g = 2.01. Therefore, it is expected that the electron-deficient Pt active sites (Pt^{2+}/Pt^{4+}) on AD-Pt-G ADCs may boost the catalytic ozonation compared with nanoparticular Pt (Pt^0). In addition, the actual Pt loadings of 0.25AD-Pt-G, 0.5AD-Pt-G, and 1.0AD-Pt-G were measured as 0.23, 0.44, and 0.99 wt % by ICP-OES, respectively.

To verify the oxidation states and configuration structures of the Pt species on AD-Pt-G catalysts, XAFS analysis was conducted. As shown in Figure 2c, the normalized Pt L$_3$-edge X-ray absorption near-edge structure (XANES) spectra reveal that the white line intensities of as-prepared AD-Pt-G samples are between those of Pt foil and PtO$_2$, illustrating that the valence states of atomic Pt on AD-Pt-G are between 0 and +4.[22,37] Fourier transform extended X-ray absorption fine structure (FT-EXAFS) spectra were conducted to further analyze the atomic coordination signature of Pt on AD-Pt-G samples. As shown in Figure 2d, a strong peak at *ca.* 1.5 Å (without correction) corresponding to the Pt−C bond can be observed for both 0.5AD-Pt-G and 1.0AD-Pt-G, suggesting the strong Pt−C interaction between atomic Pt and the graphene support.[38,39] In addition, the peaks located at 2−3 Å (without correction) can be attributed to the Pt−Pt bond derived from Pt$_2$ dimers on 0.5AD-Pt-G or Pt dimers/nanoparticles on 1.0AD-Pt-G.[38,39] To identify the coordination environment around the atomic Pt species, the FT-EXAFS of 0.5AD-Pt-G and 1.0AD-Pt-G were fitted in R space, as shown in Figure 2e,. The fitting results (Table S1) indicate coordination numbers of 3.0 and 2.6 for the first shell of Pt atoms on 0.5AD-Pt-G and 1.0AD-Pt-G, respectively, which may be ascribed to the stabilization of atomic Pt by three C atoms on single carbon defect to construct the Pt$_x$C$_3$ coordination structure. In addition, the calculated coordination number of Pt−Pt bonds on 1.0AD-Pt-G is 3.4, much larger than that of 0.5AD-Pt-G, which is consistent with the larger proportion of Pt nanoparticles on 1.0AD-Pt-G identified by HAADF-STEM (Figure S4). Obviously, both XAFS and XPS analyses confirm the abundance of positively charged atomic Pt species (Pt^{2+}/Pt^{4+}) deposits on graphene via a Pt−C bond to construct the Pt$_x$C$_3$ configuration, which are beneficial to promoting the utilization of active sites and catalytic reactions due to the EMSI-constructed uneven electron distribution.

3.2. Catalytic Ozonation of CH$_3$SH Using AD-Pt-G Catalysts.

The performance of catalytic ozonation to remove CH$_3$SH over the as-prepared AD-Pt-G catalysts was evaluated and is depicted in Figure 3. First, only 17.8% of CH$_3$SH removal is achieved by sole ozonation (Figure 3a), whereas 60.6% of CH$_3$SH removal is achieved within a 30 min adsorption for 0.5AD-Pt-G in air (0.5AD-Pt-G/air process in Figure 3c). In catalytic ozonation, as shown in Figure 3a, with respect to AD-Pt-G, in the initial period, the catalytic degradation efficiency increases significantly, and then the catalytic degradation trend reaches a relatively stable trend during the 30−180 min period. This is because the concentration of CH$_3$SH in the reaction system decreases rapidly due to the catalytic degradation of AD-Pt-G and then quickly decreases to their minimum values along with time extension. Within a 180 min reaction, 0.5AD-Pt-G can realize a removal efficiency of 97.5% for 50 ppm of CH$_3$SH, significantly higher than those of 1.0AD-Pt-G (79.1%), 0.25AD-Pt-G

(43.3%), 0.5NP-Pt-G (62.3%), and PG (39.6%), verifying that graphene-supported atomically dispersed Pt catalysts can readily facilitate the catalytic ozonation to remove CH$_3$SH. The improved CH$_3$SH removal efficiency with the increase in the Pt content from 0.25 to 0.5 wt % can be ascribed to the increased atomic active sites of Pt$_x$C$_3$ configuration on the catalysts. However, 1.0AD-Pt-G with a higher Pt loading content and 0.5NP-Pt-G with abundant Pt nanoparticles show a lower CH$_3$SH removal performance than 0.5AD-Pt-G, indicating that the formation of Pt nanoclusters or nanoparticles may reduce the catalytic ozonation activity.[17,40] In addition, the normalized CH$_3$SH removal of per mg Pt values for different graphene-supported Pt catalysts (Figure S10) are 72.6 and 78.2 μmol for 0.25AD-Pt-G and 0.5AD-Pt-G with atomic Pt species, respectively, much higher than those of 1.0AD-Pt-G (31.8 μmol) and 0.5NP-Pt-G (49.1 μmol) with metallic Pt nanoparticles, further implying the high Pt utilization and efficient CH$_3$SH removal ability of positively charged atomic Pt species on graphene nanosheets even at a lower Pt loading for the optimum 0.5AD-Pt-G.

Since the mutual interaction between atomic Pt species and the support needs to be considered for elaborating the EMSI effect, commercial carbon nanotubes (CNTs) and graphitic carbon nitride (g-C$_3$N$_4$) were also used to deposit atomic Pt for CH$_3$SH elimination in catalytic ozonation. As shown in Figure 3b, 0.5AD-Pt-G shows the best CH$_3$SH removal efficiency (97.5%) in catalytic ozonation compared to 0.5Pt-CNTs (84.2%) and 0.5Pt-g-C$_3$N$_4$ (40.9%), which may be ascribed to the stronger EMSI effect of Pt$_x$C$_3$ configuration induced by the covalent Pt−C bond between atomic Pt and graphene as well as the favorable physicochemical properties of graphene including a higher conductivity and abundant carbon defects.[24,41] These results illustrate the advantages of carbon defects on graphene for anchoring atomically dispersed Pt, which can not only stabilize the atomic Pt but also construct a stronger EMSI effect to regulate the electronic properties of catalysts, thus improving its O$_3$ activation ability.

In order to further confirm the ability of AD-Pt-G to activate O$_3$, the CH$_3$SH removal performance of 0.5AD-Pt-G was then investigated under nitrogen, air, and ozone atmospheres. As shown in Figure 3c, the CH$_3$SH removal efficiency after 30 min for 0.5AD-Pt-G/O$_3$ (98.4%) is much higher than those for 0.5AD-Pt-G/air (60.6%) and 0.5AD-Pt-G/N$_2$ (22.0%), confirming the catalytic ozonation ability of AD-Pt-G catalysts. Especially, 0.5AD-Pt-G/air shows a higher efficiency than 0.5AD-Pt-G/N$_2$, indicating that the atomic Pt species on 0.5AD-Pt-G can probably activate O$_2$ for the removal of CH$_3$SH. This is because the atomically dispersed Pt$_x$C$_3$ configuration with uneven charge density distribution has a strong activation ability for O$_2$ and O$_3$, thus boosting its catalytic performance.[34,35] In addition, the optimum mass of the catalyst (0.1 g) and the relative humidity (RH = 65%) have been identified for 0.5AD-Pt-G (Figures S11 and S12) for the following experiments.

To comprehensively evaluate the potential of the as-obtained AD-Pt-G catalysts in practical application, the O$_3$ concentration in outlet gas was monitored to investigate whether the residual O$_3$ causes secondary pollution. Figure 3d indicates that 99.94% O$_3$ conversion efficiency is realized by the 0.5AD-Pt-G/O$_3$ process with a residual O$_3$ concentration of less than 0.04 ppm (meeting China Ambient Air Quality Standards, 0.2 mg m^{-3}, ≈0.094 ppm), suggesting the high utilization rate of O$_3$ during catalytic ozonation. In addition,
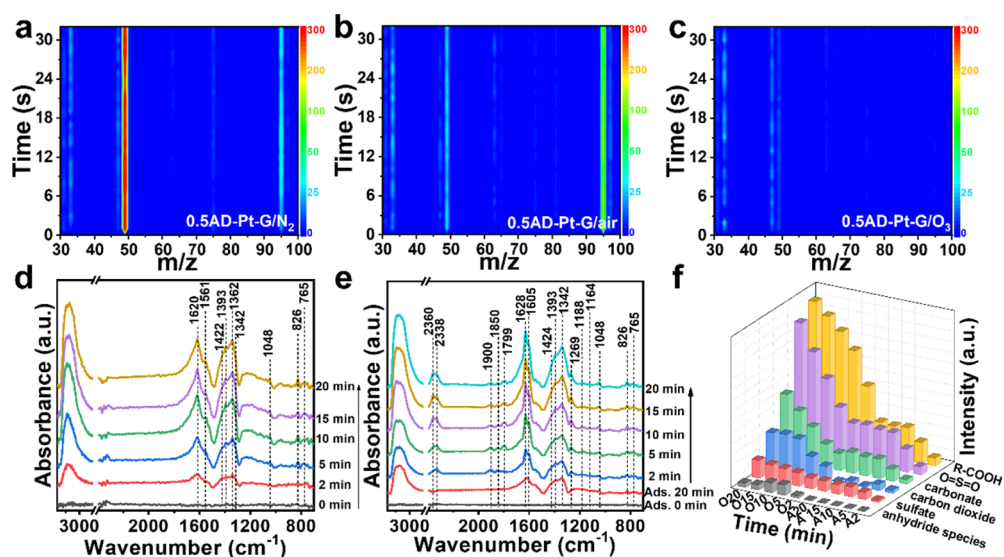
Figure 4. Concentration of identified typical volatile organic products in PTR-ToF-MS for CH_3SH removal by the (a) 0.5AD-Pt-G/N_2, (b) 0.5AD-Pt-G/air, or (c) 0.5AD-Pt-G/O_3 process after 30 min. *In situ* DRIFTS in the process of (d) adsorption and (e) catalytic ozonation over 0.5AD-Pt-G. (f) Normalized spectra of *in situ* DRIFTS (A and O represent the adsorption and catalytic ozonation processes, respectively).

the humidity resistance and stability of catalysts for VOCs elimination are also important for their industrial applications. Therefore, the effect of different relatively humidities (RH) on CH_3SH removal efficiency by catalytic ozonation over the as-prepared AD-Pt-G catalysts was investigated. As shown in Figure S12, AD-Pt-G catalysts can maintain a relatively stable CH_3SH removal activity in catalytic ozonation under different humidities. In particular, 0.5AD-Pt-G can maintain a satisfactory catalytic performance under extreme atmospheric conditions, with CH_3SH removal efficiencies of 76.7% and 85.8% under RH < 5% and RH > 95%, respectively. As for the durability, as shown in Figure 3e, the 0.5AD-Pt-G/O_3 process achieves a CH_3SH removal efficiency of 91.5% within a 12 h reaction, still higher than those of PG/O_3 (40.4%) and individual O_3 (17.2%) processes. Especially, no evidence associated with the formation of Pt nanoparticles is observed in the XRD spectra and SEM, TEM, and HAADF-STEM images at different magnifications for the used 0.5AD-Pt-G (Figures S13 and S14), suggesting an excellent stability of atomic Pt on AD-Pt-G catalysts. Since the activity declined to 48.7% after a 48 h reaction (Figure S15), the XPS (Figure 3f, Figure S16, and Table S2) and FTIR (Figure S17) results indicate that the deactivation is probably due to the oxidation of atomic Pt^{2+} species (Pt^{2+} ratio decrease from 76.60 to 63.32%) and the accumulation of sulfur- and carbon-containing oxidation products. Hence, two strategies were carried out to regenerate the catalysts and investigate the main reason for deactivation. The regenerated catalysts after washing exhibit a removal efficiency of 58.5% after a 180 min reaction, whereas the regenerated catalysts by annealing in a N_2 atmosphere exhibit an obvious recoverable removal efficiency of 96.5%, suggesting that the main deactivation reason could be related to the oxidation of the active Pt_xC_3 sites. Fortunately, the catalysts can be regenerated and reused via the simple annealing method to remove the accumulated products and reduce the oxidized Pt^{4+} species into active Pt^{2+} species. Furthermore, the catalytic performance of 0.5AD-Pt-G for CH_3SH removal is superior to most metal oxide-based catalysts reported previously, including MnO_2- and CuO-based catalysts (Table S3), further revealing the potential industrial application of

graphene-supported atomically dispersed Pt catalysts with a strong EMSI effect in catalytic ozonation for air purification.

3.3. Intermediates and Final Products of CH_3SH Elimination. In order to analyze the conversion pathway of CH_3SH after adsorption and catalytic ozonation over 0.5AD-Pt-G, the intermediates and products of CH_3SH were systematically identified. First, the volatile compounds in the exhaust gas after reaction were analyzed by PTR-ToF-MS. The identified typical products based on the detected m/z patterns for different cases (Figure S18) are displayed in Table S4. Figure 4a−c shows the concentration of identified typical volatile organic products during CH_3SH removal in 0.5AD-Pt-G/N_2, 0.5AD-Pt-G/air, and 0.5AD-Pt-G/O_3 processes. Only weak signals of CH_3SH can be detected at m/z = 49.01 for 0.5AD-Pt-G/air and 0.5AD-Pt-G/O_3 processes, while obvious peaks of CH_3SH still survive for the 0.5AD-Pt-G/N_2 process, indicating the efficient CH_3SH removal using 0.5AD-Pt-G in the presence of air or O_3 rather than N_2, consistent with the above activity test results. In addition, a higher concentration of CH_3SSCH_3 and limited CH_3SH are detected in the 0.5AD-Pt-G/air process, whereas a trace amount of CH_3SSCH_3 is detected in the 0.5AD-Pt-G/N_2 process, further confirming that AD-Pt-G ADCs can activate molecular O_2 for CH_3SH oxidation. As reported, Pt^{2+} species can activate O_2 and transform into Pt^{4+} adsorbed with active oxygen species, and the formed Pt^{4+} species are liable to extract electrons from VOCs directly, resulting in the partial oxidation of CH_3SH during adsorption under an air atmosphere.[29,42] In contrast, during the 0.5AD-Pt-G/O_3 process, the signals of CH_3SH and oxidation intermediates (CH_3SSCH_3, HCOOH, etc.) become weaker and even undetectable as the reaction proceeds (Figure S19), suggesting that CH_3SH is completely decomposed into inorganic final products. Next, the inorganic products including CO_2 and SO_4^{2-} after CH_3SH mineralization were also analyzed. The concentrations of CO_2 in the outlet gas during adsorption and catalytic ozonation were measured, and the calculated mineralization rates are shown in Figure S20. In the catalytic ozonation process, the mineralization rate reaches the highest 47.0% at 105 min and maintains at 35.3% after a 180 min reaction, whereas in the adsorption process, the

mineralization rate only reaches 16.47% at 45 min (the highest value during the adsorption process) and declines to 2.35% after 180 min. The sulfur oxides including SO_4^{2-} and $CH_3SO_3^-$ on 0.5AD-Pt-G after adsorption and catalytic ozonation were detected by ion chromatography (IC). As shown in Figure S21, tiny amounts of SO_4^{2-} and $CH_3SO_3^-$ are formed in the adsorption process using 0.5AD-Pt-G under an air atmosphere, proving the incomplete mineralization of CH_3SH during adsorption, whereas higher concentrations of SO_4^{2-} and $CH_3SO_3^-$ ions are detected in the 0.5AD-Pt-G/O_3 process, revealing that catalytic ozonation over 0.5AD-Pt-G provides a deeper oxidation and mineralization of sulfur in CH_3SH. Hence, the higher CO_2 and SO_4^{2-} formation in catalytic ozonation over AD-Pt-G comprehensively indicates the higher mineralization and deeper oxidation degree of CH_3SH in the AD-Pt-G/O_3 process, resulting from the efficient oxidation ability of O_3 activation on AD-Pt-G.

To gain deeper insights into the decomposition pathway during SVOCs elimination, in situ DRIFTS experiments were performed to analyze the interface reaction between catalysts and CH_3SH. The IR spectra during the adsorption process are shown in Figure 4d. Upon exposure to the mixture of N_2 and CH_3SH, the peak of $\nu(C-S)$ associated to CH_3SH appears at 765 cm^{-1}, whereas no peak in a range of 2500−2600 cm^{-1} (due to $\nu(S-H)$) is observed, suggesting the fast adsorption and transformation of CH_3SH into CH_3SSCH_3 on AD-Pt-G, in line with the detection of CH_3SSCH_3 in PTR-ToF-MS.[43,44] Simultaneously, the appearance of peaks relevant to C−O−S bonds at 826 cm^{-1}, sulfate species at 1048 and 1362 cm^{-1} for $\nu(SO_3)$ and $\nu(O=S=O)$, and sulfonate species at 1342 cm^{-1} for $\nu(O=S=O)$ as well as the generation of carbonate, bicarbonate, and HCOOH species at 1422, 1620, and 1561 cm^{-1} indicates the breaking of C−S of CH_3SH and further oxidation after its adsorption on 0.5AD-Pt-G.[44,45] These observed peaks indicate the direct oxidation of CH_3SH on 0.5AD-Pt-G, with the formation of sulfur- and carbon-containing oxides during the CH_3SH adsorption process.

After introducing ozone into CH_3SH-containing feed stream, similar bands related to the oxidative products but with a higher intensity are observed as the process prolongs, suggesting a more intensive oxidation during the catalytic ozonation process using 0.5AD-Pt-G (Figure 4e). The emerging new peaks of sulfonate ions ($\nu(SO_3)$) at 1164 and 1188 cm^{-1} as well as the increased peak of sulfate ions (SO_4^{2-}) at 1048 cm^{-1} suggest that sulfonate and sulfate ions are the final oxidation products adsorbed on the AD-Pt-G surface.[46] Combining with the PTR-ToF-MS results, it can be considered that the sulfur element in CH_3SH undergoes the cleavage of the S−H bond, partial oxidation into CH_3SSCH_3, organo-sulfates, and sulfonate species, and final oxidation to sulfate ions after cleavage of the C−S bond during catalytic ozonation. As for the carbon element, the new absorption bands at 1900, 1850, and 1799 cm^{-1} ascribed to $\nu(C=O)$ of anhydride species increase first and then decrease, which are probably derived from anhydride intermediates during the oxidation of alcohol to acid.[47] Moreover, the blue-shifted and intensely obvious peak at 1605 cm^{-1} ($\nu_{as}(COO)$ of formic acid species) and the new peak at 1269 cm^{-1} ($\nu_{as}(COO)$ of bidentate carbonates species) indicate that the fast oxidation of CH_3SH leads to the rapid formation of acid and carbonates species on the AD-Pt-G surface.[14,48] Notably, the bands at 2360 and 2338 cm^{-1} are attributed to gaseous CO_2, while the peak at 1629 cm^{-1} represents the H_2O molecules, which illustrates the final

mineralization of CH_3SH into CO_2 and H_2O.[48−50] The above observed peaks reveal that the carbon element of CH_3SH undergoes the evolution of aldehydes, carboxylic acid, and carbonates species and is finally oxidized into harmless CO_2 after catalytic ozonation over 0.5AD-Pt-G.

According to the normalized IR spectra (Figure 4f), it can be found that certain peaks representing oxidation products (including organosulfates, carboxylic acids, and carbonates species) appear during the adsorption process, and the reaction equilibrium is achieved within 10 min due to the absence of O_2/O_3. Once purged with ozone, the deeper oxidation products including CO_2 and sulfate ions increase obviously, confirming the boosting oxidation in catalytic ozonation. In addition, the XPS result (Figure S16 and Table S2) shows that the proportion of residual sulfur oxides on the used 0.5AD-Pt-G increases from 44.44 to 57.60% after air and O_3 purging, respectively. The results of PTR-ToF-MS, in situ FTIR, and XPS collectively confirm the mineralization of CH_3SH into SO_4^{2-} and CO_2/H_2O via catalytic ozonation over AD-Pt-G ADCs.

3.4. Atomic Oxygen and Reactive Oxygen Species Analysis. Generally, catalytic ozonation can greatly lead to the formation of surface adsorbed oxygen species, which further transform into other reactive oxygen species (ROS, ·OH, ·O_2^-, $^1O_2$, etc.) involved in catalytic reactions.[13] Hence, in situ Raman was first used to investigate the generated surface adsorbed oxygen species on AD-Pt-G catalysts in the presence of O_2 or O_3. As shown in Figure 5a, compared with 0.5AD-Pt-
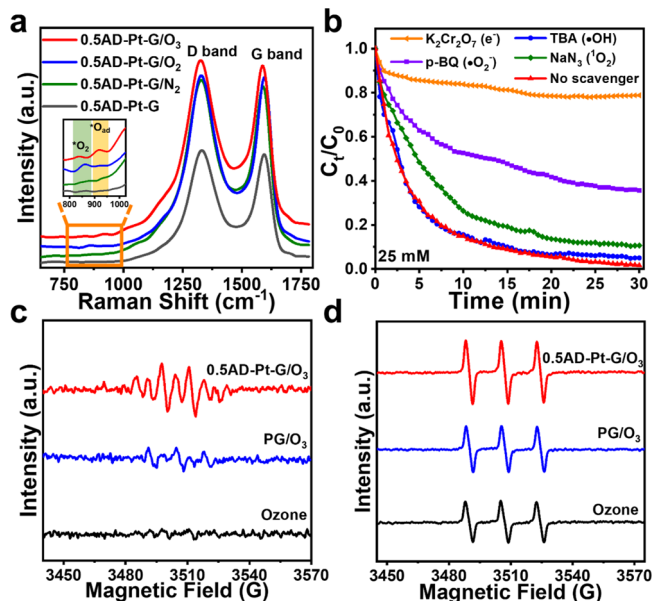

Figure 5. (a) In situ Raman spectra of 0.5AD-Pt-G under various atmospheres. (b) Catalytic ozonation activity for CH_3SH removal of 0.5AD-Pt-G quenched by 25 mM scavengers. ESR spectra of (c) ·O_2^- and (d) $^1O_2$ in different processes.

G under a N_2 atmosphere, a new band appears at 862 cm^{-1} after exposure to O_2, which can be ascribed to the formation of peroxide species (*O_2) due to the activation of O_2 by atomic Pt^{2+}.[51,52] In contrast, the obvious signals at 918 and 838 cm^{-1} for 0.5AD-Pt-G under the O_3 atmosphere indicate the simultaneous formation of surface atomic oxygen species (*O_{ad}) and *O_2, suggesting that O_3 is activated by atomic Pt^{2+} on 0.5AD-Pt-G and transform into *O_{ad} and *O_2.[26,51] The

surface oxygen species including $*O_{ad}$ (oxidation−reduction potential (ORP) = 2.43 V) and $*O_2$ (ORP = 1.35 V) can participate in the elimination of CH_3SH through direct oxidation due to their oxidation ability and even transform into ROS such as $\cdot OH$, $\cdot O_2^-$, $^1O_2$, etc.[53] Hence, the transformed ROS has been collectively identified by scavenger study and electron spin resonance (ESR) analysis.[54,55] As shown in Figure 5b and Figure S22, there is no significant quenching effect in the removal of CH_3SH after adding TBA and NaN_3, suggesting that $\cdot OH$ and $^1O_2$ can be ignored in the 0.5AD-Pt-G/O_3 system. In contrast, the addition of p-BQ reduces the removal efficiency to 48.68%, indicating that $\cdot O_2^-$ participates actively in the catalytic ozonation for CH_3SH removal. Especially, the addition of $K_2Cr_2O_7$ (electron quencher) greatly inhibits the removal efficiency to 11.48%, proving the critical role of electron transfer in catalytic ozonation over 0.5AD-Pt-G, which may be attributed to the nonradical reaction derived from surface $*O_{ad}$ oxidation and the direct electron transfer between higher valent Pt and CH_3SH.[29,53] Coincidentally, the enhanced signals of DMPO-$\cdot O_2^-$ and TEMP-$^1O_2$ adducts were observed over 0.5AD-Pt-G/O_3 compared to the sole ozonation and PG/O_3 process (ESR analysis in Figure 5c,d), confirming that the Pt_xC_3-based EMSI effect accelerates the decomposition of O_3 and the formation of $\cdot O_2^-$/$^1O_2$ during catalytic ozonation. In addition, Figure S23 demonstrates that neither O_3 alone nor catalytic ozonation displays the characteristic signal of the DMPO-$\cdot OH$ adducts, proving the trace concentration of $\cdot OH$ in the 0.5AD-Pt-G/O_3 system. Combined with the results of scavenger study and ESR results, it can be inferred that $\cdot O_2^-$ is the critical ROS in the 0.5AD-Pt-G/O_3 process. It can be concluded that O_3 is decomposed into $*O_{ad}$ and $*O_2$ to directly oxidize CH_3SH or convert into $\cdot O_2^-$ for CH_3SH elimination during catalytic ozonation over 0.5AD-Pt-G.

3.5. Catalytic Mechanism. DFT calculations were carried out to further reveal the mechanism for the catalytic ozonation activity over AD-Pt-G ADCs. Considering the EXAFS fitting results and STEM images of 0.5AD-Pt-G, Pt_xC_3 coordination including Pt_1C_3, Pt_2C_3, and Pt_4C_3 structures are constructed as the atomic Pt species including mainly single Pt_1 atoms, Pt_2 dimers, and a small number of clusters on 0.5AD-Pt-G.[24,56] Figure S24 illustrates that these atomic Pt species located above the carbon defect lead to a significant lattice deformation of graphene. In addition, the uneven charge density in Figure 6a−c illustrates the charge transfer of the Pt−C bond in Pt_xC_3 configuration due to the EMSI effect between atomic Pt and the graphene support, consistent with the solid-state EPR analysis (Figure 2b). As reported, after devoting charges to the adjacent C atoms, the constructed electron-deficient Pt^{2+} sites exhibit a stronger ability to adsorb O_3 molecules owing to the Lewis basicity of the terminal oxygen atom of O_3.[26,27] Therefore, the uneven charge density distribution induced by EMSI can promote the catalytic ozonation performance of 0.5AD-Pt-G.

Subsequently, the adsorption energies (E_{ad}) for O_3 and O_2 adsorbed on Pt_1C_3, Pt_2C_3, and Pt_4C_3 configuration structures were calculated. As shown in Figure 6d−g, Figure S25, and Table 1, the calculated E_{ad} values for O_3 on Pt_1C_3, Pt_2C_3, and Pt_4C_3 are −2.73, −2.16, and −2.24 eV, respectively, whereas the E_{ad} values for O_2 on Pt_1C_3, Pt_2C_3, and Pt_4C_3 are −2.58, −1.55, and −2.08 eV, respectively, indicating that Pt_1C_3 coordination exhibits the strongest O_3 and O_2 adsorption ability in these models. In addition, the Pt(111) surface is also
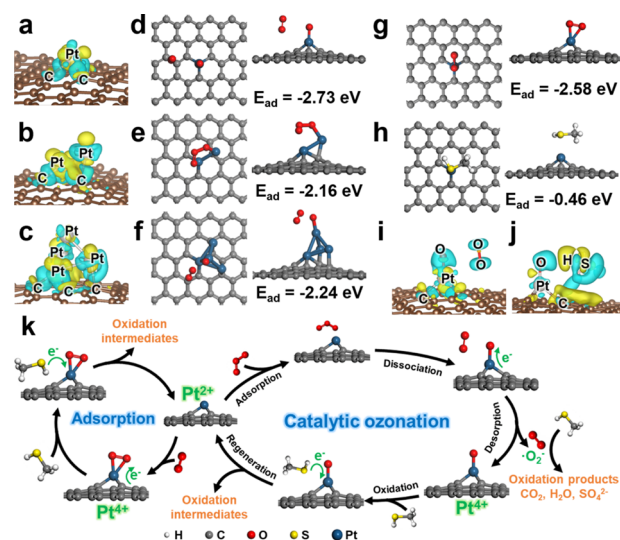

Figure 6. Charge difference iso-surfaces and the optimized adsorption of O_3 molecule on (a, d) Pt_1C_3, (b, e) Pt_2C_3, and (c, f) Pt_4C_3 models. Optimized adsorption of (g) O_2 and (h) CH_3SH molecules on Pt_1C_3 coordination. Charge difference iso-surfaces of (i) Pt_1C_3 after adsorption of O_3 and (j) Pt_1C_3-$*O_{ad}$ after adsorption of CH_3SH. Cyan and light yellow represent electron accumulation and electron-deficient regions, respectively. (k) Proposed reaction mechanism for CH_3SH elimination using AD-Pt-G during adsorption and catalytic ozonation.

Table 1. Adsorption Energy and Bond Length of O_2 and O_3 Molecules Adsorbed on Different Coordination Structures of AD-Pt-G

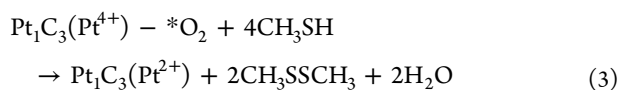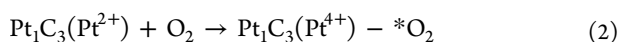| structure	O_2 adsorption energy (eV)	L_{O1-O2} of O_2 (Å)	O_3 adsorption energy (eV)	L_{O1-O2} of O_3 (Å)	L_{O2-O3} of O_3 (Å)
Pt_1C_3	−2.58	1.450	−2.73	3.241	1.254
Pt_2C_3	−1.55	1.299	−2.16	1.447	1.362
Pt_4C_3	−2.08	1.313	−2.24	1.783	1.249
Pt(111)			−2.05	1.407	1.408
molecule		1.236		1.286	1.286

designed as the model for nanoparticular Pt (Pt_{NP}) to compare the O_3 activation ability between Pt_{NP} and atomic Pt species. E_{ad} for O_3 on Pt_xC_3 is stronger than that of Pt(111) (−2.05 eV), indicating that the O_3 adsorption activity of the atomic Pt species is better than that of Pt_{NP} (Figure S26). Since Pt_1C_3 presents the strongest O_3 and O_2 adsorption ability among these Pt_xC_3 models, Pt_1C_3 is chosen as the typical structure for further DFT analysis. After adsorption, the length of O_2 molecules adsorbed on Pt_1C_3 configuration increases to 1.450 Å as well as an O−O bond in O_3 is also greatly enlarged to 3.241 Å, suggesting the easier cleavage O−O bond of O_2 and O_3 on Pt_1C_3 configuration to form $*O_{ad}$/$*O_2$ species to participate in the oxidation.[57,58] The deformation charge density of Pt_1C_3 adsorbed with O_3 (Figure 6i) also illustrates that charges transfer from atomic Pt to the O_3 molecule, and the O_3 molecule is decomposed into a free $*O_2$ and an $*O_{ad}$ remaining on Pt sites after accepting electrons. The $*O_2$ species can convert into $\cdot O_2^-$ to participate in the oxidation of CH_3SH along with $*O_{ad}$, consistent with in situ Raman and ESR results (Figure 5). The lower adsorption energies, obvious deformation of molecules, and large quantities of electron transfer prove that the positively charged Pt species on AD-Pt-

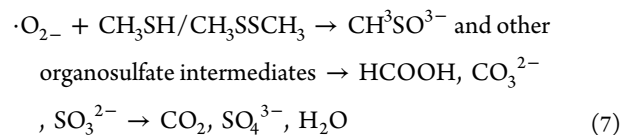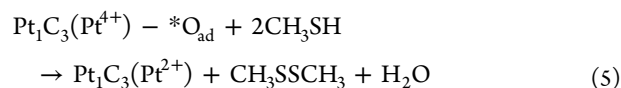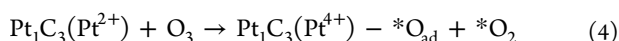G are favorable to activate the O_3 molecule for catalytic ozonation.

As for CH_3SH, the calculated E_{ad} for CH_3SH in the Pt_1C_3 configuration structure was −0.46 eV, weaker than those for O_3 and O_2, indicating that Pt_1C_3 prefers to adsorb O_3 and O_2 molecules compared to CH_3SH in catalytic ozonation. Moreover, the cycling of Pt^{2+} species after activating O_3 is crucial for the catalytic stability of AD-Pt-G. After devoting electrons to O_3, the atomic Pt^{2+} sites tend to convert into Pt^{4+} adsorbing ROS (Pt_1C_3-*O_{ad}), which can probably adsorb and capture electrons from CH_3SH strongly.[29,42] Hence, the deformation charge density of Pt_1C_3-*O_{ad} after CH_3SH adsorption (Figure 6j) indicates that the electrons of H and S atoms in CH_3SH are transferred to O and Pt atoms in the Pt_1C_3-*O_{ad} site. This result suggests the electron compensation of the atomic Pt^{4+} sites on AD-Pt-G from CH_3SH oxidation, thus promoting the cycle of Pt^{4+} into Pt^{2+} during the catalytic ozonation process. The XPS analysis of 0.5AD-Pt-G used after CH_3SH adsorption and catalytic ozonation could provide the collateral evidence, as presented in Figure 3f and Table S2. The depletion of Pt^{2+} (from 72.02 to 63.32%) after catalytic ozonation confirms the key role of Pt^{2+} in the decomposition of O_3 into *O_{ad}/*O_2/·O_2^-, whereas the increase in Pt^{2+} (from 72.02 to 76.60%) after CH_3SH adsorption may be ascribed to the cycle from Pt^{4+} to Pt^{2+} via direct electron transfer of CH_3SH, which is predicted by the above DFT calculation. The cycle of Pt^{2+}/Pt^{4+} can also maintain the stability of AD-Pt-G by avoiding the aggregation of Pt^0.[22]

As discussed above, the possible reaction mechanism for CH_3SH elimination during adsorption and catalytic ozonation using AD-Pt-G can be proposed as the following equation and Figure 6k, taking the optimum Pt_1C_3 coordination as a typical example. First, the strong EMSI between atomic Pt and graphene leads to the positively charged state (Pt^{2+}) of Pt_1C_3 configuration. The relatively electron-deficient atomic Pt^{2+} can capture and activate O_2 in air, thus partially oxidizing CH_3SH during the adsorption process (eqs 2 and 3). Second, similar to Lewis acid sites, the atomic Pt^{2+} exhibits a boosting adsorption/activation ability for O_3, which can decompose the adsorbed O_3 into *O_{ad}/*O_2 by donating electrons to O_3 and converting itself into Pt^{4+} species (eq 4). The generated *O_2 can further transform into ·O_2^- to collectively oxidize CH_3SH (eqs 6 and 7). Finally, atomic Pt^{4+} can convert back into Pt^{2+} species via direct electron transfer between Pt^{4+} and CH_3SH, thus achieving the redox cycles of $Pt^{2+} \rightarrow Pt^{4+} \rightarrow Pt^{2+}$ and accomplishing the regeneration of Pt active sites (eq 5). After donating the electrons to Pt^{4+} species and oxidized by ROS, CH_3SH can be oxidized into final inorganic oxidation products. The construction of Pt^{2+}/Pt^{4+} at Pt_1C_3 with unoccupied 5d-orbitals plays a significant role in the fast activation of O_3 and rapid circulation of active sites, thus boosting the performance of catalytic ozonation for CH_3SH removal.

Under an air atmosphere:

$$Pt_1C_3(Pt^{2+}) + O_2 \rightarrow Pt_1C_3(Pt^{4+}) - *O_2 \qquad (2)$$

$$Pt_1C_3(Pt^{4+}) - *O_2 + 4CH_3SH$$
$$\rightarrow Pt_1C_3(Pt^{2+}) + 2CH_3SSCH_3 + 2H_2O \qquad (3)$$

Under an O_3 atmosphere:

$$Pt_1C_3(Pt^{2+}) + O_3 \rightarrow Pt_1C_3(Pt^{4+}) - *O_{ad} + *O_2 \qquad (4)$$

$$Pt_1C_3(Pt^{4+}) - *O_{ad} + 2CH_3SH$$
$$\rightarrow Pt_1C_3(Pt^{2+}) + CH_3SSCH_3 + H_2O \qquad (5)$$

$$*O^2 \rightarrow ·O^{2-} \qquad (6)$$

$$·O_{2-} + CH_3SH/CH_3SSCH_3 \rightarrow CH^3SO^{3-} \text{ and other}$$
$$\text{organosulfate intermediates} \rightarrow HCOOH, CO_3^{2-}$$
$$, SO_3^{2-} \rightarrow CO_2, SO_4^{3-}, H_2O \qquad (7)$$

3.6. Environmental Implication. In this study, graphene-supported atomically dispersed Pt catalysts (AD-Pt-G) were designed and utilized for CH_3SH removal in catalytic ozonation. The boosting catalytic ozonation performance of AD-Pt-G can be ascribed to the positively charged Pt sites (Pt^{2+}/Pt^{4+}) of the Pt_xC_3-based strong EMSI effect. The constructed redox pair of Pt^{2+}/Pt^{4+} can maintain high activity during long-term tests via fast circulation, with ~90% removal efficiency up to 12 h under a GHSV of 60,000 mL h^{-1}. AD-Pt-G catalysts can be applied in large-scale odor treatment facilities based on catalytic ozonation technology for deodorization in sewage treatment and petroleum plants. In addition, AD-Pt-G can be loaded on a filter or nonwoven fabric via hot-pressing, which can be used as air purifier accessories or masks for portable deodorizing equipment. This work can shed light on the development of high-efficiency and low-cost catalytic ozonation catalysts and lays a foundation for the large-scale applications of catalytic ozonation in SVOCs elimination and air purification in the future.

■ ASSOCIATED CONTENT

ⓈⒾ Supporting Information

The Supporting Information is available free of charge at https://pubs.acs.org/doi/10.1021/acs.est.1c06938.

> Experimental supplementary section (Texts S1−S11), fitting parameters in the Pt L_3-edge FT-EXAFS (Table S1), XPS analysis of 0.5AD-Pt-G in fresh and after adsorption and catalytic ozonation (Table S2), comparison of CH_3SH removal performance over previously reported catalysts (Table S3), detected products in PTR-ToF-MS (Table S4), TEM and HAADF-STEM images for 0.5AD-Pt-G, 0.25AD-Pt-G and 1.0AD-Pt-G (Figures S1−S4), XRD and TEM images for 0.5NP-Pt-G (Figure S5), XPS and Raman spectra for samples (Figures S6−S9), supplementary performances in catalytic ozonation of CH_3SH over AD-Pt-G samples (Figures S10−S12 and S15), XRD, SEM, TEM, STEM, XPS, and FTIR analyses of 0.5AD-Pt-G before and after catalytic ozonation (Figures S13, S14, S16, and S17), PTR-ToF-MS spectra and detected inorganic products for CH_3SH removal in various processes by 0.5AD-Pt-G (Figures S18−S21), supplementary scavenger and EPR results (Figures S22 and S23), optimum structure of Pt_xC_3 (Figure S24), and DFT calculations over Pt_xC_3 and Pt(111) (Figures S25 and 26) (PDF)

■ AUTHOR INFORMATION

Corresponding Author

Dehua Xia − *School of Environmental Science and Engineering, Sun Yat-sen University, Guangzhou 510275, China; Guangdong Provincial Key Laboratory of Environmental Pollution Control and Remediation*

Technology, Guangzhou 510275, China; ● orcid.org/0000-0001-6016-358X; Phone: +86 20 39332690; Email: xiadehua3@mail.sysu.edu.cn

Authors

Yajing Huang − *School of Environmental Science and Engineering, Sun Yat-sen University, Guangzhou 510275, China;* ● orcid.org/0000-0002-4333-8859

Dingren Ma − *School of Environmental Science and Engineering, Sun Yat-sen University, Guangzhou 510275, China*

Weiqi Liu − *School of Environmental Science and Engineering, Sun Yat-sen University, Guangzhou 510275, China*

Lingling Hu − *School of Environmental Science and Engineering, Sun Yat-sen University, Guangzhou 510275, China*

Jingling Yang − *School of Environment, Jinan University, Guangzhou 510632, China*

Peng Liao − *State Key Laboratory of Environmental Geochemistry, Institute of Geochemistry, Chinese Academy of Sciences, Guiyang 550081, PR China;* ● orcid.org/0000-0001-6924-1097

Chun He − *School of Environmental Science and Engineering, Sun Yat-sen University, Guangzhou 510275, China; Guangdong Provincial Key Laboratory of Environmental Pollution Control and Remediation Technology, Guangzhou 510275, China;* ● orcid.org/0000-0002-3875-5631

Complete contact information is available at:
https://pubs.acs.org/10.1021/acs.est.1c06938

Notes

The authors declare no competing financial interest.

■ REFERENCES

(1) He, D.; Zhao, Y.; Yang, S.; Mei, Y.; Yu, J.; Liu, J.; Chen, D. K.; He, S.; Luo, Y. Enhancement of catalytic performance and resistance to carbonaceous deposit of lanthanum (La) doped HZSM-5 catalysts for decomposition of methyl mercaptan. *Chem. Eng. J.* **2018**, *336*, 579−586.

(2) Yang, J.; Huang, Y.; Chen, Y. W.; Xia, D.; Mou, C. Y.; Hu, L.; Zeng, J.; He, C.; Wong, P. K.; Zhu, H. Y. Active site-directed tandem catalysis on CuO/V_O-MnO₂ for efficient and stable catalytic ozonation of S-VOCs under mild condition. *Nano Today* **2020**, *35*, 100944.

(3) Hanajima, D.; Kuroda, K.; Morishita, K.; Fujita, J.; Maeda, K.; Morioka, R. Key odor components responsible for the impact on olfactory sense during swine feces composting. *Bioresour. Technol.* **2010**, *101*, 2306−2310.

(4) Colom-Diaz, J. M.; Alzueta, M. U.; Zeng, Z.; Altarawneh, M.; Dlugogorski, B. Z. Oxidation of H₂S and CH₃SH in a jet-stirred reactor: Experiments and kinetic modeling. *Fuel* **2021**, *283*, 119258.

(5) He, D.; Yu, J.; Mei, Y.; Liu, J.; Zhao, Y.; Yang, S.; Cao, X.; He, S.; Luo, Y. The effects of Cr addition in HZSM-5 on its structure, physicochemical and catalytic properties for methyl mercaptan abatement. *Catal. Commun.* **2018**, *112*, 31−34.

(6) Zhang, S. Y.; Long, Y. Y.; Fang, Y.; Du, Y.; Liu, W. J.; Shen, D. S. Effects of aeration and leachate recirculation on methyl mercaptan emissions from landfill. *Waste Manage.* **2017**, *68*, 337−343.

(7) Bashkova, S.; Bagreev, A.; Bandosz, T. J. Adsorption of methyl mercaptan on activated carbons. *Environ. Sci. Technol.* **2002**, *36*, 2777−2782.

(8) Yang, J.; Xu, W.; He, C.; Huang, Y.; Zhang, Z.; Wang, Y.; Hu, L.; Xia, D.; Shu, D. One-step synthesis of silicon carbide foams supported hierarchical porous sludge-derived activated carbon as efficient odor gas adsorbent. *J. Hazard. Mater.* **2018**, *344*, 33−41.

(9) Lebrero, R.; Rodriguez, E.; Estrada, J. M.; Garcia-Encina, P. A.; Munoz, R. Odor abatement in biotrickling filters: Effect of the EBRT on methyl mercaptan and hydrophobic VOCs removal. *Bioresour. Technol.* **2012**, *109*, 38−45.

(10) Zhao, S.; Yi, H.; Tang, X.; Gao, F.; Zhang, B.; Wang, Z.; Zuo, Y. Methyl mercaptan removal from gas streams using metal-modified activated carbon. *J. Cleaner Prod.* **2015**, *87*, 856−861.

(11) Liu, T. X.; Li, X. Z.; Li, F. B. AgNO₃-induced photocatalytic degradation of odorous methyl mercaptan in gaseous phase: Mechanism of chemisorption and photocatalytic reaction. *Environ. Sci. Technol.* **2008**, *42*, 4540−4545.

(12) Sano, T.; Koike, K.; Hori, T.; Hirakawa, T.; Ohko, Y.; Takeuchi, K. Removal of methyl mercaptan with highly-mobile silver on graphitic carbon-nitride (g-C₃N₄) photocatalyst. *Appl. Catal., B* **2016**, *198*, 133−141.

(13) Xia, D.; Xu, W.; Wang, Y.; Yang, J.; Huang, Y.; Hu, L.; He, C.; Shu, D.; Leung, D. Y. C.; Pang, Z. Enhanced performance and conversion pathway for catalytic ozonation of methyl mercaptan on single-atom Ag deposited three-dimensional ordered mesoporous MnO₂. *Environ. Sci. Technol.* **2018**, *52*, 13399−13409.

(14) Wang, H. C.; Huang, Z. W.; Jiang, Z.; Zhang, Y.; Zhang, Z. X.; Shangguan, W. F. Trifunctional C@MnO catalyst for enhanced stable simultaneously catalytic removal of formaldehyde and ozone. *ACS Catal.* **2018**, *8*, 3164−3180.

(15) Kwong, C. W.; Chao, C. Y. H.; Hui, K. S.; Wan, M. P. Catalytic ozonation of toluene using zeolite and MCM-41 materials. *Environ. Sci. Technol.* **2008**, *42*, 8504−8509.

(16) Rezaei, E.; Soltan, J.; Chen, N.; Lin, J. Effect of noble metals on activity of MnOₓ/gamma-alumina catalyst in catalytic zonation of toluene. *Chem. Eng. J.* **2013**, *214*, 219−228.

(17) Tian, M.; Liu, S.; Wang, L.; Ding, H.; Zhao, D.; Wang, Y.; Cui, J.; Fu, J.; Shang, J.; Li, G. K. Complete degradation of gaseous methanol over Pt/FeOₓ catalysts by normal temperature catalytic ozonation. *Environ. Sci. Technol.* **2020**, *54*, 1938−1945.

(18) Yang, W. W.; Bunian, M.; Chen, X. K.; Heald, S.; Yu, L.; Wen, J. G.; Lei, Y.; Wu, T. T. Plasmon-enhanced catalytic ozonation for efficient removal of recalcitrant water pollutants. *ACS EST Engg.* **2021**, *1*, 874−883.

(19) Zhou, P.; Lv, F.; Li, N.; Zhang, Y.; Mu, Z.; Tang, Y.; Lai, J.; Chao, Y.; Luo, M.; Lin, F.; Zhou, J.; Su, D.; Guo, S. Strengthening reactive metal-support interaction to stabilize high-density Pt single atoms on electron-deficient g-C₃N₄ for boosting photocatalytic H₂ production. *Nano Energy* **2019**, *56*, 127−137.

(20) Kuang, P.; Wang, Y.; Zhu, B.; Xia, F.; Tung, C. W.; Wu, J.; Chen, H. M.; Yu, J. Pt single atoms supported on N-doped mesoporous hollow carbon spheres with enhanced electrocatalytic H₂-evolution activity. *Adv. Mater.* **2021**, *33*, 9.

(21) Ye, X.; Wang, H.; Lin, Y.; Liu, X.; Cao, L.; Gu, J.; Lu, J. Insight of the stability and activity of platinum single atoms on ceria. *Nano Res.* **2019**, *12*, 1401−1409.

(22) Li, J.; Guan, Q.; Wu, H.; Liu, W.; Lin, Y.; Sun, Z.; Ye, X.; Zheng, X.; Pan, H.; Zhu, J.; Chen, S.; Zhang, W.; Wei, S.; Lu, J.

Highly active and stable metal single-atom catalysts achieved by strong electronic metal-support interactions. *J. Am. Chem. Soc.* **2019**, *141*, 14515−14519.

(23) Lou, Y.; Xu, J.; Wu, H.; Liu, J. Hollow carbon anchored highly dispersed Pd species for selective hydrogenation of 3-nitrostyrene: metal-carbon interaction. *Chem. Commun.* **2018**, *54*, 13248−13251.

(24) Yao, Y. G.; Huang, Z. N.; Xie, P. F.; Wu, L. P.; Ma, L.; Li, T. Y.; Pang, Z. Q.; Jiao, M. L.; Liang, Z. Q.; Gao, J. L.; He, Y.; Kline, D. J.; Zachariah, M. R.; Wang, C. M.; Lu, J.; Wu, T. P.; Li, T.; Wang, C.; Shahbazian, R.; Hu, L. B. High temperature shockwave stabilized single atoms. *Nat. Nanotechnol.* **2019**, *14*, 851−857.

(25) Wang, Y.; Cao, H.; Chen, L.; Chen, C.; Duan, X.; Xie, Y.; Song, W.; Sun, H.; Wang, S. Tailored synthesis of active reduced graphene oxides from waste graphite: Structural defects and pollutant-dependent reactive radicals in aqueous organics decontamination. *Appl. Catal., B* **2018**, *229*, 71−80.

(26) Bing, J.; Hu, C.; Nie, Y.; Yang, M.; Qu, J. Mechanism of catalytic ozonation in Fe₂O₃/Al₂O₃@SBA-15 aqueous suspension for destruction of ibuprofen. *Environ. Sci. Technol.* **2015**, *49*, 1690−1697.

(27) Yu, G.; Wang, Y.; Cao, H.; Zhao, H.; Xie, Y. Reactive oxygen species and catalytic active sites in heterogeneous catalytic ozonation for water purification. *Environ. Sci. Technol.* **2020**, *54*, 5931−5946.

(28) Chen, X. X.; Zhan, S. J.; Chen, D. S.; He, C.; Tian, S. H.; Xiong, Y. Grey Fe-CeO₂-sigma for boosting photocatalytic ozonation of refractory pollutants: Roles of surface and bulk oxygen vacancies. *Appl. Catal., B* **2021**, *286*, 14.

(29) Li, Q.; Li, Z.; Zhang, Q.; Zheng, L.; Yan, W.; Liang, X.; Gu, L.; Chen, C.; Wang, D.; Peng, Q.; Li, Y. Porous γ-Fe₂O₃ nanoparticle decorated with atomically dispersed platinum: Study on atomic site structural change and gas sensor activity evolution. *Nano Res.* **2020**, *14*, 1435−1442.

(30) Lightcap, I. V.; Kosel, T. H.; Kamat, P. V. Anchoring semiconductor and metal nanoparticles on a two-dimensional catalyst mat. storing and shuttling electrons with reduced graphene oxide. *Nano Lett.* **2010**, *10*, 577−583.

(31) Qu, Y.; Chen, B.; Li, Z.; Duan, X.; Wang, L.; Lin, Y.; Yuan, T.; Zhou, F.; Hu, Y.; Yang, Z.; Zhao, C.; Wang, J.; Zhao, C.; Hu, Y.; Wu, G.; Zhang, Q.; Xu, Q.; Liu, B.; Gao, P.; You, R.; Huang, W.; Zheng, L.; Gu, L.; Wu, Y.; Li, Y. Thermal emitting strategy to synthesize atomically dispersed Pt metal sites from bulk Pt metal. *J. Am. Chem. Soc.* **2019**, *141*, 4505−4509.

(32) Jiang, K.; Liu, B. Y.; Luo, M.; Ning, S. C.; Peng, M.; Zhao, Y.; Lu, Y. R.; Chan, T. S.; de Groot, F. M. F.; Tan, Y. W. Single platinum atoms embedded in nanoporous cobalt selenide as electrocatalyst for accelerating hydrogen evolution reaction. *Nat. Commun.* **2019**, *10*, 9.

(33) Xi, J. B.; Sung, H. Y.; Wang, D.; Zhang, Z. Y.; Duan, X. M.; Xiao, J. W.; Xiao, F.; Liu, L. M.; Wang, S. Confined-interface-directed synthesis of Palladium single-atom catalysts on graphene/amorphous carbon. *Appl. Catal., B* **2018**, *225*, 291−297.

(34) Yan, X.; Duan, P.; Zhang, F.; Li, H.; Zhang, H. X.; Zhao, M.; Zhang, X.; Xu, B.; Pennycook, S.; Guo, J. Stable single-atom platinum catalyst trapped in carbon onion graphitic shells for improved chemoselective hydrogenation of nitroarenes. *Carbon* **2019**, *143*, 378−384.

(35) Zhang, J.; Zhao, Y.; Chen, C.; Huang, Y. C.; Dong, C. L.; Chen, C. J.; Liu, R. S.; Wang, C.; Yan, K.; Li, Y.; Wang, G. Tuning the coordination environment in single-atom catalysts to achieve highly efficient oxygen reduction reactions. *J. Am. Chem. Soc.* **2019**, *141*, 20118−20126.

(36) Sathe, B. R.; Zou, X.; Asefa, T. Metal-free B-doped graphene with efficient electrocatalytic activity for hydrogen evolution reaction. *Catal. Sci. Technol.* **2014**, *4*, 2023−2030.

(37) Liu, J.; Jiao, M.; Mei, B.; Tong, Y.; Li, Y.; Ruan, M.; Song, P.; Sun, G.; Jiang, L.; Wang, Y.; Jiang, Z.; Gu, L.; Zhou, Z.; Xu, W. Carbon-supported divacancy-anchored platinum single-atom electrocatalysts with superhigh Pt utilization for the oxygen reduction reaction. *Angew. Chem. Int. Edit.* **2019**, *58*, 1163−1167.

(38) Kim, J. H.; Shin, D.; Lee, J.; Baek, D. S.; Shin, T. J.; Kim, Y. T.; Jeong, H. Y.; Kwak, J. H.; Kim, H.; Joo, S. H. A General Strategy to Atomically Dispersed Precious Metal Catalysts for Unravelling Their Catalytic Trends for Oxygen Reduction Reaction. *ACS Nano* **2020**, *14*, 1990−2001.

(39) Tian, S.; Wang, B.; Gong, W.; He, Z.; Xu, Q.; Chen, W.; Zhang, Q.; Zhu, Y.; Yang, J.; Fu, Q.; Chen, C.; Bu, Y.; Gu, L.; Sun, X.; Zhao, H.; Wang, D.; Li, Y. Dual-atom Pt heterogeneous catalyst with excellent catalytic performances for the selective hydrogenation and epoxidation. *Nat. Commun.* **2021**, *12*, 3181.

(40) Zeng, Z.; Su, Y.; Quan, X.; Choi, W.; Zhang, G.; Liu, N.; Kim, B.; Chen, S.; Yu, H.; Zhang, S. Single-atom platinum confined by the interlayer nanospace of carbon nitride for efficient photocatalytic hydrogen evolution. *Nano Energy* **2020**, *69*, 104409.

(41) Wang, J.; Chen, S.; Quan, X.; Yu, H. Fluorine-doped carbon nanotubes as an efficient metal-free catalyst for destruction of organic pollutants in catalytic ozonation. *Chemosphere* **2018**, *190*, 135−143.

(42) Maurer, F.; Jelic, J.; Wang, J.; Gaenzler, A.; Dolcet, P.; Woell, C.; Wang, Y.; Studt, F.; Casapu, M.; Grunwaldt, J.-D. Tracking the formation, fate and consequence for catalytic activity of Pt single sites on CeO₂. *Nat. Catal.* **2020**, *3*, 824−833.

(43) Zhao, S.; Yi, H.; Tang, X.; Kang, D.; Gao, F.; Wang, J.; Huang, Y.; Yang, Z. Removal of volatile odorous organic compounds over NiAl mixed oxides at low temperature. *J. Hazard. Mater.* **2018**, *344*, 797−810.

(44) Nishino, N.; Arquero, K. D.; Dawson, M. L.; Finlayson-Pitts, B. J. Infrared studies of the reaction of methanesulfonic acid with trimethylamine on surfaces. *Environ. Sci. Technol.* **2014**, *48*, 323−330.

(45) Pereira, L.; Amado, A. M.; Critchley, A. T.; van de Velde, F.; Ribeiro-Claro, P. J. A. Identification of selected seaweed poly-saccharides (phycocolloids) by vibrational spectroscopy (FTIR-ATR and FT-Raman). *Food Hydrocolloids* **2009**, *23*, 1903−1909.

(46) He, C.; Wang, Y.; Li, Z.; Huang, Y.; Liao, Y.; Xia, D.; Lee, S. Facet engineered alpha-MnO₂ for efficient catalytic ozonation of odor CH₃SH: oxygen vacancy-induced active centers and catalytic mechanism. *Environ. Sci. Technol.* **2020**, *54*, 12771−12783.

(47) Lochar, V.; Drobna, H. FTIR study of the interaction of crotonaldehyde and maleic anhydride with V₂O₅ and MoO₃. *Appl. Catal., A* **2004**, *269*, 27−31.

(48) Zhao, D. Z.; Shi, C.; Li, X. S.; Zhu, A. M.; Jang, B. W. L. Enhanced effect of water vapor on complete oxidation of form-aldehyde in air with ozone over MnOₓ catalysts at room temperature. *J. Hazard. Mater.* **2012**, *239*, 362−369.

(49) Chen, B. B.; Shi, C. A.; Crocker, M.; Wang, Y.; Zhu, A. M. Catalytic removal of formaldehyde at room temperature over supported gold catalysts. *Appl. Catal., B* **2013**, *132*, 245−255.

(50) Chen, H.; Kong, L.; Chen, J.; Zhang, R.; Wang, L. Heterogeneous uptake of carbonyl sulfide on hematite and hematite-NaCl mixtures. *Environ. Sci. Technol.* **2007**, *41*, 6484−6490.

(51) Kang, L.; Wang, B.; Bing, Q.; Zalibera, M.; Buchel, R.; Xu, R.; Wang, Q.; Liu, Y.; Gianolio, D.; Tang, C. C.; Gibson, E. K.; Danaie, M.; Allen, C.; Wu, K.; Marlow, S.; Sun, L. D.; He, Q.; Guan, S.; Savitsky, A.; Velasco-Velez, J. J.; Callison, J.; Kay, C. W. M.; Pratsinis, S. E.; Lubitz, W.; Liu, J. Y.; Wang, F. R. Adsorption and activation of molecular oxygen over atomic copper(I/II) site on ceria. *Nat. Commun.* **2020**, *11*, 4008.

(52) Jia, J.; Zhang, P.; Chen, L. Catalytic decomposition of gaseous ozone over manganese dioxides with different crystal structures. *Appl. Catal., B* **2016**, *189*, 210−218.

(53) Bing, J.; Hu, C.; Zhang, L. Enhanced mineralization of pharmaceuticals by surface oxidation over mesoporous gamma-Ti-Al₂O₃ suspension with ozone. *Appl. Catal., B* **2017**, *202*, 118−126.

(54) Xia, D.; Liu, H.; Xu, B.; Wang, Y.; Liao, Y.; Huang, Y.; Ye, L.; He, C.; Wong, P. K.; Qiu, R. Single Ag atom engineered 3D-MnO₂ porous hollow microspheres for rapid photothermocatalytic inactivation of *E. coli* under solar light. *Appl. Catal., B* **2019**, *245*, 177−189.

(55) Xia, D.; He, H.; Liu, H.; Wang, Y.; Zhang, Q.; Li, Y.; Lu, A.; He, C.; Wong, P. K. Persulfate-mediated catalytic and photocatalytic bacterial inactivation by magnetic natural ilmenite. *Appl. Catal., B* **2018**, *238*, 70−81.

(56) Chen, W.; Luo, X.; Slater, T. J. A.; Zhou, Y.; Ling, S.; Bao, R.; Alves Fernandes, J.; Wang, J.; Shen, Y. General synthesis of single atom electrocatalysts via a facile condensation-carbonization process. *J. Mater. Chem. A* **2020**, *8*, 25959−25969.

(57) Liu, J.; Jiao, M. G.; Lu, L. L.; Barkholtz, H. M.; Li, Y. P.; Wang, Y.; Jiang, L. H.; Wu, Z. J.; Liu, D. J.; Zhuang, L.; Ma, C.; Zeng, J.; Zhang, B. S.; Su, D. S.; Song, P.; Xing, W.; Xu, W. L.; Jiang, Z.; Sun, G. Q. High performance platinum single atom electrocatalyst for oxygen reduction reaction. *Nat. Commun.* **2017**, *8*, 9.

(58) Ma, R.; Lin, G.; Ju, Q.; Tang, W.; Chen, G.; Chen, Z.; Liu, Q.; Yang, M.; Lu, Y.; Wang, J. Edge-sited Fe-N$_4$ atomic species improve oxygen reduction activity via boosting O$_2$ dissociation. *Appl. Catal., B* **2020**, *265*, 9.